Research Article | Vol. 28, No. 26 / 21 December 2020 / Optics Express 39868
Optics EXPRESS

Computation of canting errors in heliostats by flux map fitting: experimental assessment

ALBERTO SÁNCHEZ-GONZÁLEZ,[1,*] BENJAMIN GRANGE,[2] AND CYRIL CALIOT[2,3]

[1] *Energy Systems Engineering (ISE) Group, Department of Thermal and Fluid Engineering, Universidad Carlos III de Madrid, Av. Universidad, 30, 28911 Leganés, Madrid, Spain*
[2] *Processes, Materials and Solar Energy Laboratory, PROMES-CNRS, 7 rue du Four Solaire, 66120 Font-Romeu-Odeillo-Via, France*
[3] *Universite de Pau et des Pays de l'Adour, E2S UPPA, CNRS, LMAP, Pau, France*
[*] *asgonzal@ing.uc3m.es*

Abstract: In solar tower plants, thousands of heliostats reflect sunlight into a central receiver. Heliostats consist of a subset of mirrors called facets that must be perfectly oriented (i.e., canted) to concentrate as much solar radiation as possible. This study presents and validates the so-called flux map fitting technique to detect and correct canting errors. The computed distributions were matched to a series of images through an optimization algorithm. According to the sensitivity analysis, three images spread along a single day provide sufficient information for the algorithm to succeed. Using this methodology, four heliostats at the THEMIS research facility were recanted, thereby substantially increasing the optical quality in three of them. The procedure to infer the heliostat aimpoint was assessed.

1. Introduction

The alignment of optical systems is crucial for proper operation. The importance of alignment is evident in reflecting systems involving mirrors. Alignment is required not only in imaging systems, such as telescopes [1,2], but also in non-imaging systems, whose goal is to collect or concentrate light [3] rather than image formation. This is the case of concentrating solar power (CSP) systems, which concentrate solar radiation into a receiver [4].

Thousands of heliostats (i.e., tracking mirrors) concentrate sunrays onto a receiver at the top of a tower in solar power tower (SPT) plants, for which the final output generally is the electricity generated from a sun-heated fluid [5]. Heliostats consist of an array of mirrors called facets. Owing to solar beam divergence [6,7], heliostat mirror facets must be aligned to concentrate the maximum possible solar radiation.

Heliostat mirror facet alignment entails two operations: focusing and canting. Mirror focusing is the slight bending of the facet surface into a concave shape. Heliostat canting involves tilting each facet to direct the reflected sunlight at a single aimpoint. Figure 1 shows a graphical representation of both an uncanted (left) and a canted (right) heliostat. When the on-axis is aligned, the normal vectors of all the facets cross at the center of a virtual sphere of radius $2f_h$, where f_h is the focal length of the heliostat. In on-axis alignment, when the sun is in line with the heliostat center and the focal point (i.e., the receiver), the flux concentration at the focal point is maximum.

As a result of proper heliostat alignment, the spot size and spillage losses at the receiver are reduced. Consequently, the optical efficiency of the heliostat field is enhanced, and the annual power intercepted by the receiver is maximized [8].

Heliostat facet alignment is performed not only in plant commissioning but also throughout its lifetime. Permanent deformation of the heliostat structure together with the progressive

#412116 https://doi.org/10.1364/OE.412116
Journal © 2020 Received 12 Oct 2020; revised 1 Dec 2020; accepted 1 Dec 2020; published 16 Dec 2020

Optics EXPRESS

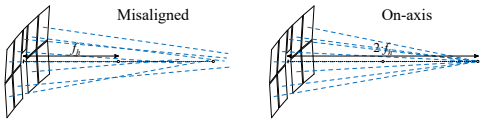

Fig. 1. Schematic of misaligned (left) vs. on-axis canted (right) heliostats.

loosening of screw nuts for canting adjustment give rise to the need for detection and correction of alignment errors.

Methods for heliostat facet canting are grouped into three categories [9,10]: on-sun, mechanical, and optical. In on-sun alignment, single facets are individually adjusted by visual inspection of the beam shape on the target. This qualitative technique is imprecise and time-consuming. Mechanical alignment techniques make use of gauge blocks or inclinometers placed on the facets while in horizontal position. This procedure, which is commonly employed in SPT plants, is more accurate but requires extensive resources, especially in terms of time and personnel.

In the optical category, six canting techniques can be identified: laser method, photogrammetry, camera look-back, backward gazing, target reflection, and flux map fitting. The laser method uses a collimated laser beam reflected by the heliostat facets. Although it is accurate, the laser method requires a lot of time and expensive equipment [9]. The photogrammetry method estimates the orientation of the facets from a series of images of the heliostat. Photogrammetry is also very time-consuming and not very accurate [11]. The camera look-back method uses the self-reflection of the camera on the heliostat facets [12]; this technique is accurate but time-consuming too [13]. The backward gazing method uses cameras to capture the sun image through its reflection on the heliostat; local slope and canting errors can be inferred from this technique [4]. The target reflection method compares actual and theoretical images of the reflection of a known target on the heliostat facets [14]. A commercial implementation of the target reflection method, which is not time-consuming, is known as H-FACET [13].

The present study is devoted to the last aforementioned optical technique: flux map fitting [15]. In this technique, a series of heliostat images in the white target is confronted against an optical model, in which canting errors act as degrees of freedom. Through optimization, canting errors are found when the computed flux maps fit the measured flux maps for a set of heliostat orientations.

The main goal of the present study was to assess the flux map fitting technique by means of extensive field validation. Before validation, a sensitivity analysis was performed on the selection of raw images: number and time period between them. The reliability of the technique using a 3-image series was evaluated through an experimental campaign involving four heliostats at THEMIS, a solar-tower research facility operated by the CNRS-PROMES laboratory. The procedure to infer the aimpoint was also assessed by comparison with the increments in encoder counts.

The manuscript is structured as follows. The methodology behind the flux map fitting technique is first described. A sensitivity analysis on the selection of image series is then reported. Subsequently, an experimental campaign over four heliostats is presented, together with the methodology applied to compute the canting errors. Subsequently, the verification of the aimpoint inference against encoder data is reported. Then, the methodology applied to the corrected facets is described, and the optical quality improvement experimentally evaluated in this study is reported. Finally, a discussion and comparison with raytracing simulations are provided, and conclusions are drawn from the findings.

Optics EXPRESS

2. Methodology

In this section, we propose an optimization method to quantify canting errors. The optical model for flux mapping is then presented, followed by a procedure to infer the aimpoint position in the white target. All the procedures presented in this section were implemented in a computational code that serves as the core of the methodology. Further details on the methodology can be found in Ref. [15].

2.1. Optimization: fitting flux maps to experiments

The technique is based on matching the flux distributions from an optical model to those experimentally obtained on the white target. The canting errors (δ), which are the unknowns to be determined, act as degrees of freedom in the optical model. By means of an optimization algorithm, canting errors in each heliostat facet are found through this technique's code.

The code, originally programmed in MATLAB, is fed by a series of experimental images of the heliostat under study. For several time instants, a CCD camera takes images of the flux distribution concentrated on the white target placed at the top of the tower. As the white Lambertian target reflects diffusively in all directions [16], the image captured by the camera provides information on the intensity level (L). The 16-bit camera employed in this study provides up to 65536 levels. The specific value of L in each pixel divided by the maximum level on an image (L_{max}) is equivalent to the normalized flux density (F), ranging from 0 to 1. Using this normalization, the model eliminates the local flux density (FD) in W/m^2, which ultimately depends on unknown loss factors such as the mirror local reflectivity and atmospheric attenuation. Further information on raw image treatment can be found in Ref. [15].

$$F = \frac{FD}{FD_{max}} \equiv \frac{L}{L_{max}} \tag{1}$$

A cost function (to be maximized) needs to be defined for the optimization procedure; it must be independent of the size of the spot, which varies throughout the day. In pattern recognition, the cross-correlation coefficient (CCC) is usually employed, e.g., in [17]. In the present study, the CCC, also known as Pearson correlation coefficient, is defined according to Eq. (2), where F is the 3D matrix of normalized flux densities for all time instants in the series, N_{elts} is the number of elements (i.e., number of pixels times the number of images); SD is the standard deviation; and the *exp* and *mod* subscripts stand for experimental and model, respectively.

$$CCC = \frac{1}{N_{elts}-1}\sum_{n=1}^{N_{elts}}\left(\frac{F_{\mathrm{exp},n}-\overline{F_{\mathrm{exp}}}}{SD\left(F_{\mathrm{exp}}\right)}\right)\left(\frac{F_{\mathrm{mod},n}-\overline{F_{\mathrm{mod}}}}{SD\left(F_{\mathrm{mod}}\right)}\right) \tag{2}$$

The optimization algorithm is responsible for finding the unknowns (canting errors) that maximize the objective function (CCC). The main requirement for the algorithm is to find the global (or nearly global) optimum in a deterministic manner, independent of starting points or parameter tuning. The DIRECT (DIviding RECTangles) algorithm was previously found to meet such requirements [15].

The DIRECT optimization algorithm, originally presented by Jones et al. [18], sequentially divides the dimensions of the search space into thirds, and selects the ones that maximize the objective function. We adopted the code implementation of DIRECT in Ref. [19].

2.2. Flux mapping

In addition to the optimization algorithm, the code relies on an optical model that computes the flux distribution on the target as a function of the canting errors of the heliostat facets. From lower to higher computational cost, optical modeling tools are classified into three categories

Optics EXPRESS

[20]: convolution, cone optics, and Monte-Carlo raytracing. Given the inherent optimization cost, the convolution approach was selected.

Specifically, the convolution-projection method was utilized [21]. This model, whose GUI implementation is known as FluxSPT [22], relies on the oblique projection from the image to the target plane of an analytic function. Sun shape, concentration, and optical errors are convolved in analytic functions.

We utilized the UNIZAR function [23] at the image plane; the effective error (σ_e) is defined as formulated in Eq. (3), where ω is the incidence angle. For the sun-shape standard deviation (σ_{sun}), a value of 2.09 mrad was assigned [24,25]. However, the slope error (σ_{slp}) depends on specific heliostat mirrors and is usually missing. Thus, σ_{slp} was included in the optimization.

$$\sigma_e = \sqrt{\sigma_{sun}^2 + 2\left(1 + cos^2\omega\right)\sigma_{slp}^2} \tag{3}$$

For each heliostat facet, the convolution-projection model calculates the flux density distribution on the target with facet canting errors. By superimposing the distribution of each facet, the flux map corresponding to a heliostat is calculated at each time instant.

2.3. Aimpoint inference

As a sun-reflecting system, a heliostat is oriented so that its normal vector ($\vec{n}$) is in the bisector between the incidence vector pointing at the sun center ($\vec{s}$) and the reflected vector aiming at the target ($\vec{t}$). To compute the flux maps and determine the canting errors, it is essential to know these three vectors. If $\vec{n}$ and $\vec{s}$ are known with accuracy, $\vec{t}$ can be computed according to the reflection law:

$$\vec{t} = 2\left(\vec{s}\cdot\vec{n}\right)\vec{n} - \vec{s} \tag{4}$$

However, an accurate measurement of the sun position is usually missing. Let us remind that the sun moves at approximately 0.25 ° per minute, which is the usual temporal resolution in Almanacs such as USNO [26], the one we utilized. Accurate sun position algorithms, such as PSA [27], still require a precise clock synchronized with the camera, which was missing in the present campaign. In the absence of reliable $\vec{s}$, a procedure to infer the target $\vec{t}$ vector, or its intersection with the target plane (i.e., aimpoint), was developed.

The procedure is based on the premise that the weighted centroids of the experimental and the modeled images must coincide. The position of the aimpoint (A) on the white target can be deduced from the following three-step iterative process, shown in Fig. 2:

Step 1. Determine the centroid of the experimental image (C_{exp}).

Step 2. With aimpoint at C_{exp}, calculate the flux distribution and its centroid, C_{mod}.

Step 3. Move the aimpoint along vector $\overrightarrow{C_{mod}C_{exp}}$ in the previous step.

Taking the center of the white target (O) as reference, the aimpoint position vector ($\overrightarrow{OA}$) is obtained from the following expression:

$$\overrightarrow{OA} = 2\cdot\overrightarrow{OC_{exp}} - \overrightarrow{OC_{mod}} \tag{5}$$

where $\overrightarrow{OC_{mod}}$ denotes the position vector of the weighted centroid of the modeled distribution in step 2.

Optics EXPRESS

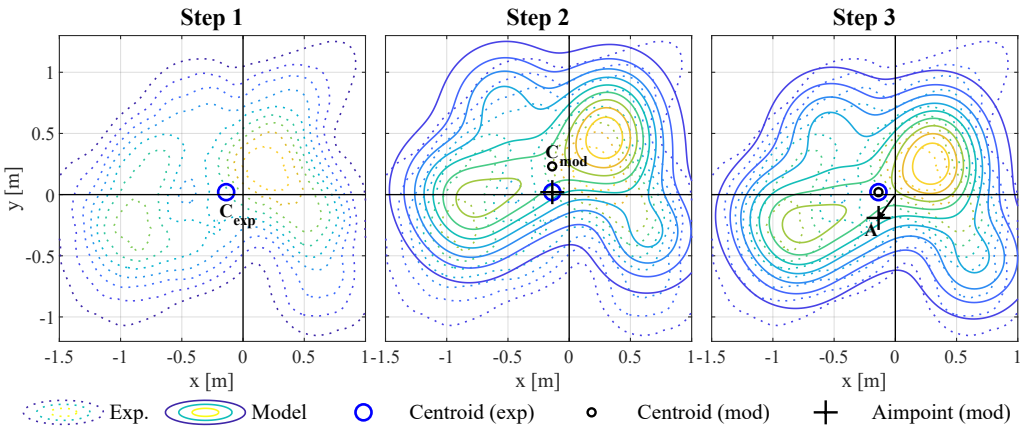

Fig. 2. Three-step process to infer the heliostat aimpoint.

3. Sensitivity analysis: selection of images

A preliminary experiment using this methodology was carried out in 2016. A single heliostat at THEMIS, heliostat A6, was tested. In this experiment, 28 images of the heliostat on the target were taken throughout a single day, from 9:54 to 17:25 local time (July 18). The 28 captured images were evenly distributed, resulting in approximately one image every 16 min [15].

Figure 3 shows the 28 time instants of image capture in central European summer time (CEST). The corresponding solar positions are represented in this figure by the angles of elevation and azimuth (with respect to the south, positive to the west). The resulting incidence angles (ω) in heliostat A6 are also depicted for the 28 time instants considered, being the lowest one at approximately 12:30.

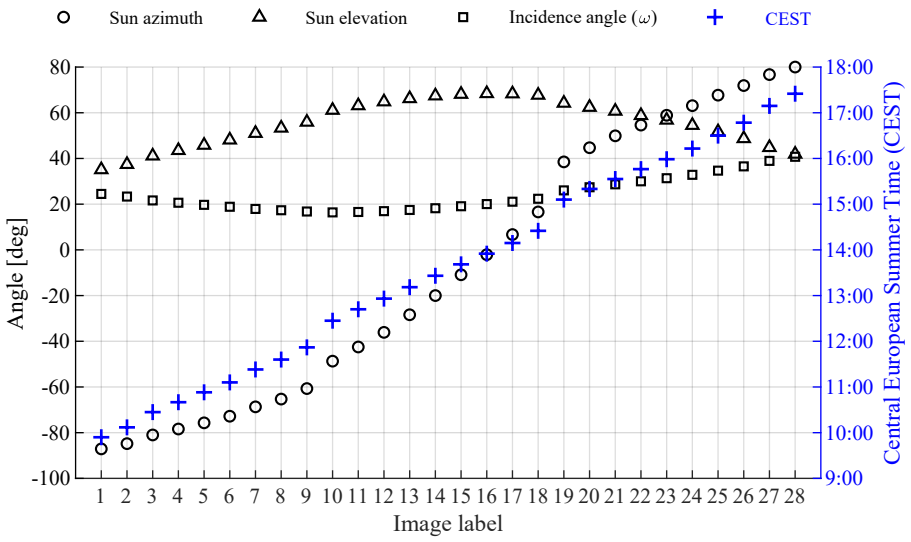

Fig. 3. Collection of 28 images: local time (right axis), solar angles, and heliostat incidence angle (left axis).

The selection of such a large series of images to feed the optimization algorithm was originally based on the reduction of uncertainty in the solution. Under commercial operation, the collection

Optics EXPRESS

of many heliostat images throughout a day leads to some loss of productivity due to the repeated defocus when aiming at the white target. Moreover, the larger the number of images is, the longer the optimization process takes. Thus, to achieve acceptable computation time, the instants and number of images need to be carefully selected.

As the sun position and heliostat incidence angle change throughout a day, the flux distribution on the target evolves over time. It is clear that the longer the time period between images within a single day, the larger the evolution. In other words, two images close together in time do not provide additional information to feed the algorithm. Consequently, the image series must consist of images spread such that a variety of sun positions and heliostat orientations are registered.

A sensitivity analysis was then performed to analyze the influence of the selection of image series. From the first collection of 28 images of heliostat A6, several sets were synthesized to compute the canting errors. Under the premise of spreading the images throughout the daytime, a different number of images were considered: 22, 18, 14, 11, 10, 9, 7, 6, 3 and 2, in addition to the original 28 images. Depending on the number of images, Table 1 lists the selected images in the set according to the image labeling in Fig. 3. This table also displays the average period of time, expressed in min, between two images in the series.

Table 1. Image series for different number of images, and average time between them.

Number of images	Selected images (labels)	Average time span [min]
2	1, 28	451
3	1, 14, 28	225
6	1, 6, 11, 16, 21, 26	82
7	1, 5, 9, 13, 17, 21, 25	66
9	1, 5, 9, 12, 16, 19, 22, 25, 28	56
10	1, 4, 7, 10, 13, 16, 19, 22, 25, 28	50
11	1, 4, 7, 9, 11, 14, 16, 19, 22, 25, 28	45
14	1, 3, 5, 7, 9, 11, 13, 15, 17, 19, 21, 23, 25, 27	33
18	1, 3, 5, 7, 9, 10, 12, 13, 15, 17, 18, 19, 21, 23, 24, 26, 27, 28	26
22	1, 2, 3, 4, 5, 6, 8, 9, 10, 12, 13, 14, 15, 17, 18, 19, 20, 22, 24, 26, 27, 28	21
28	All of them	16

Figure 4 shows the calculated canting errors depending on the number of images used to feed the optimization. For the CETHEL heliostat at THEMIS, there were 17 canting errors to be determined, as explained in the following section. These canting errors, along with the slope error, are the unknowns plotted in the horizontal axis in Fig. 4.

Broadly speaking, for some of the canting errors, usually with respect to the X-axis, the solution is quite constant regardless of the number of images; e.g., this is the case of δ_{x8} and σ_{slp}. In contrast, a certain tendency to two solutions is found for other canting errors, such as δ_{y6} and δ_{y8}.

From a closer look, note that the most atypical solution emerges when only two images are present. For a number of images greater than 2, there is no clear solution. For the sake of time saving, both in image capture and computation, a number of images equal to 3, evenly spread throughout a single day (i.e., early morning, noon, and late afternoon), was selected to perform the experimental validation in the current study.

It is important to note that the 3-image selection from this sensitivity analysis is, at most, applicable to CETHEL heliostats. For other conditions or heliostats (i.e., in terms of geometry and number of facets), the conclusions might be different.

Optics EXPRESS

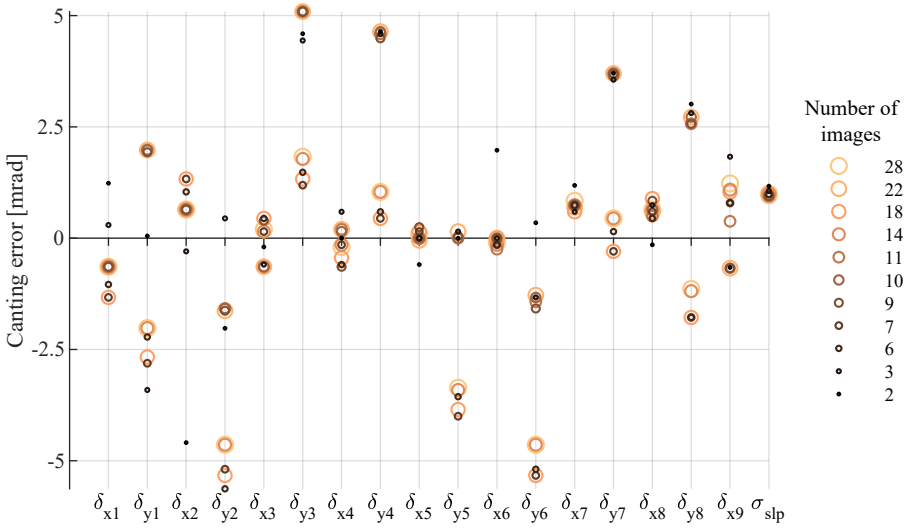

Fig. 4. Canting errors in the modules of heliostat A6 as a function of the number of images considered in the optimization.

4. Canting errors

This section presents the experimental campaign carried out to validate the proposed canting methodology extensively. The canting errors were determined for four heliostats.

4.1. Experimental campaign

An experimental campaign was carried out in the THEMIS solar-tower research facility, operated by CNRS-PROMES and located in Targassonne, France. This facility consists of a 107-heliostat field and a 104-m tower, which together serve as a research platform for SPT technology.

THEMIS heliostats, known as CETHEL, are medium-size, featuring 54 m^2 of reflective surface. The heliostat consists of two wings with 4 modules each and a central-top smaller module, i.e., nine modules in total. The term module rather than facet is utilized for the THEMIS heliostat, as each one consists of three vertical mirror strips arranged to form a quasi-spherical surface of focal length f_m, similar to common heliostat facets. Figure 5(a) shows a front view of the heliostat geometry with each module numbered.

The eight modules in the heliostat wings have two degrees of freedom for canting purposes: the horizontal and vertical axes. By means of screw-nut arrangements at the back of each module, its canting orientation can be adjusted along each axis. In the smaller central module, namely number 9, adjustment is only allowed for the X-axis.

Therefore, the CETHEL heliostat has 17 degrees of freedom, which correspond to the 17 canting errors denoted as δ_{x1}, $\delta_{y1}\cdots$, and δ_{x9}. In the absence of a canting error, i.e., on-axis alignment, the normal vector of each module ($\vec{n_m}$) is pointing at the center of a virtual sphere of radius $2f_h$. Figure 5(b) represents the local system of coordinates of the module, with indication of canting angular errors δ_x and δ_y along the X and Y axes, respectively. The sign convention for the rotation angles, which is counterclockwise positive, is also depicted in Fig. 5(b).

Four heliostats at the THEMIS heliostat field not correctly canted were selected for experimental validation. According to the field notation, the selected heliostats were A12, B6, D6, and F1. For location identification in the field, the four are labeled in the aerial view from the top of the tower shown in Fig. 6(a).

Optics EXPRESS

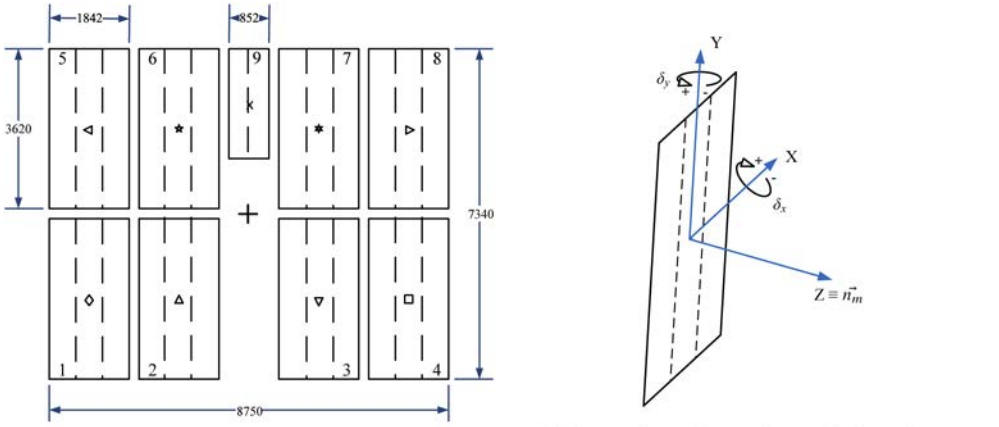

(a) Dimensions in mm. Numbered modules.

(b) System of coordinates for module's canting errors.

Fig. 5. Geometry of the CETHEL heliostat.

(a) Aerial view of the heliostat field. The four tested heliostats are labeled.

(b) Front view of heliostat D6.

Fig. 6. THEMIS heliostats.

Based on the cross-correlation coefficients presented in the foll0owing subsection, the initial optical quality of heliostat A12 was very poor, poor for heliostat B6, and fair for heliostats D6 and F1. For reference, the *CCC* between actual and ideal (on-axis alignment) images of the four selected heliostats are presented in Table 2.

Table 2. Optical characteristics of the tested heliostats and *CCC* between actual and ideal images.

Heliostat	f_h [m]	D [m]	f_m [m]	Defocus $D - f_m$ [m]	Relative defocus $(D - fm)/D$	*CCC*
A12	111.9	99.9	140	−40.1	−40.1%	0.63484
B6	85.3	69.9	100	−30.1	−43.1%	0.84594
D6	129.7	120.6	140	−19.4	−16.1%	0.88635
F1	129.7	121.0	140	−19.0	−15.7%	0.92562

The focal lengths of the heliostats (f_h) and their mirror modules (f_m) are listed in Table 2, together with the distance from each heliostat to the target point (D). This D slant range is smaller than the f_h heliostat focal length, given the position of the white target below the receiver aperture. As can be seen in Table 2, there is a significant difference between f_m and D, which

Optics EXPRESS

leads to defocus. Using a relative indicator for defocus ($(D - f_m)/D$), this effect is particularly important in heliostats A12 and B6 (the heliostats closer to the tower) with relative defocus of approximately −40%.

Moreover, some heliostats present defects in their mirrors, such as breaks, corrosion, or the lack of mirror strips. For instance, in heliostat D6, half of a mirror was absent; specifically, the bottom half of the central mirror strip in module 8, as can be seen in Fig. 6(b). The absence of mirror parts was included in the optical model; however, mirror cracks and corrosion could not be adequately modeled. In contrast to mirror cracks and corrosion, the absence of rectangular mirror parts was modeled by means of Boolean subtraction.

Heliostats are oriented to reflect the solar radiation on the white target, where the flux distribution can be inspected. The white Lambertian target is located at the tower, below the receiver aperture, 68.3 m high. The white target is a square of 7.5-m side tilted 30 ° towards the heliostat field.

The experimental flux distribution generated by the heliostat on the white target, commonly known as heliostat image, was captured by a CCD camera with appropriate filters. This camera has a resolution of 1396 x 1200 pixels, with 16384 levels (14 bits) per pixel. The same mesh grid was utilized for the computed flux maps to avoid interpolation during the fitting process.

For each heliostat, 3 images spread throughout a single day were collected, according to the previous sensitivity analysis. The acquisition of experimental images was performed on July 22.

4.2. Determination of canting errors

To determine the canting errors, the code presented in Section 3 is fed with an experimental series of 3 images collected beforehand. First, the experimental images were confronted against the flux distributions simulated by the optical model in the absence of canting errors ($\delta = 0$), i.e., on-axis alignment.

For heliostat A12, Fig. 7 (top row) shows the superposition of experimental (measured) and modeled (ideal on-axis) flux distributions at the three time instants expressed in CEST. The contours of normalized flux density (F) ranging from 0.1 to 0.9 are depicted in color lines, which are dotted and solid for the experimental and modeled distributions, respectively. In this case, the CCC is equal to 0.635, highlighting the deficient optical quality of heliostat A12, which is already noticeable from the multiple spot distribution.

The ideal alignment model distribution is taken as the starting point (zeroth iteration) in the optimization algorithm. Nevertheless, the final result is independent of the starting point, given the domain-sampling method of DIRECT optimization.

By running the code, the model distribution is fitted to the experimental one, increasing the CCC up to 0.869. As shown in the bottom row of Fig. 7, the fitting is not perfect ($CCC = 1$), but tends to reproduce the multiple spot pattern throughout the day.

Note also in Fig. 7 that the large cross symbol marks the aimpoint of the heliostat resulting from the inference procedure previously described. The remaining 9 smaller symbols (triangles, stars, etc.) are the aimpoints of each module, according to the notation in Fig. 5(a). Thus, the module producing each sub-spot can be identified. For instance, the separated spot on the left of the target is produced by module 6, as predicted by this methodology.

For heliostat A12, Visualization 1 shows a video of the flux-fitting procedure. The starting point (iteration 0) corresponds to the model without canting errors. In this example, after 50 iterations of the DIRECT algorithm, an optimal solution was found.

In addition to the previous contour figures, the code calculates the angular deviations of each module (i.e., the canting errors) and the slope error. These results are summarized in Table 3 for heliostat A12 and the other three heliostats tested. The largest canting errors were found in modules 3 and 6, in accordance with the graphical results. The sign of δ follows the convention established in Fig. 5(b).

Optics EXPRESS

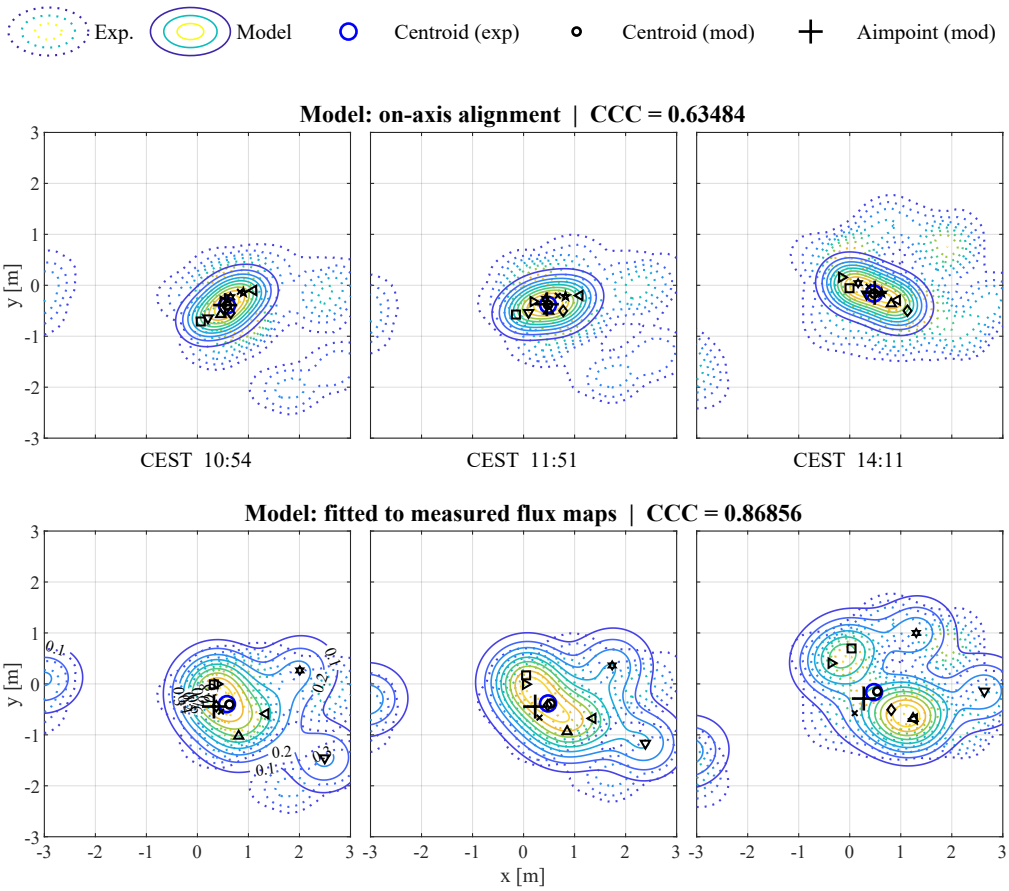

Fig. 7. Heliostat A12: experimental (dotted) and computed (solid lines) flux maps before (top) and after (bottom row) fitting. (See Visualization 1).

Table 3. Computed canting errors in the heliostat modules.

		Module								
Heliostat	[mrad]	1	2	3	4	5	6	7	8	9
A12	δ_x	−0.64	0.69	−1.83	−4.64	1.14	5.98	−5.98	−1.98	2.02
	δ_y	0.59	−3.31	−12.64	−0.64	−2.86	16.69	−5.98	0.25	$\lvert\sigma_{slp}$ = 2.25
B6	δ_x	1.07	−4.69	−3.29	−1.48	−2.39	1.07	0.25	−3.29	2.76
	δ_y	0.00	0.82	−0.33	0.25	−0.25	−2.63	3.32	−3.37	$\lvert\sigma_{slp}$ = 1.67
D6	δ_x	0.00	0.13	−0.20	0.00	0.07	−0.26	0.00	0.20	−0.41
	δ_y	−1.12	−0.26	2.70	2.04	−1.71	−1.51	0.66	0.07	$\lvert\sigma_{slp}$ = 1.17
F1	δ_x	0.26	0.00	0.66	−0.07	0.33	−0.53	0.66	−0.26	0.21
	δ_y	1.45	−4.67	0.07	−0.07	−0.92	2.63	0.26	−0.79	$\lvert\sigma_{slp}$ = 1.28

The same procedure was followed for the other three heliostats. Similar to Fig. 7, Figs. 8, 9, and 10 represent the experimental and modeled flux maps for heliostats B6, D6, and F1, respectively. Likewise, the model distributions are ideal in the three top-row images and fitted in the corresponding bottom images.

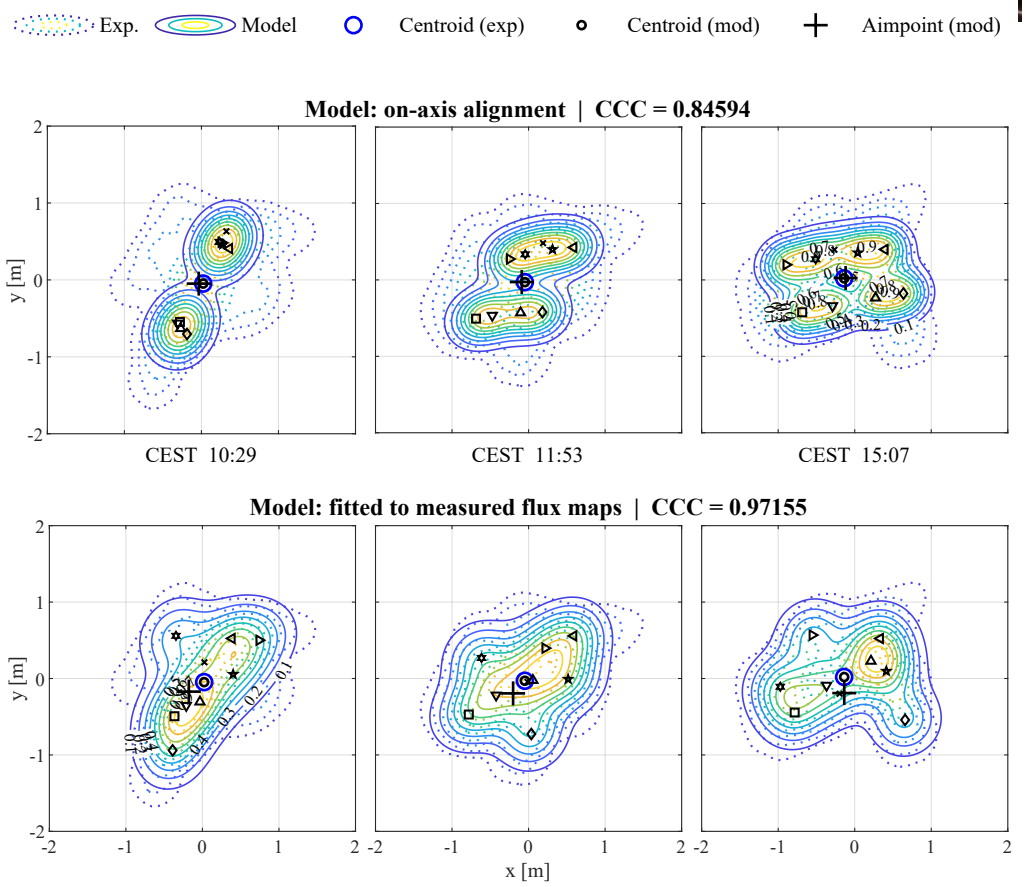

Fig. 8. Heliostat B6: experimental (dotted) and computed (solid lines) flux maps before (top) and after (bottom row) fitting.

At first, heliostat B6 presented a lower optical quality (*CCC* = 0.846), while that of heliostats D6 and F1 was better: 0.886 and 0.972, respectively. The code significantly fitted the flux maps, reaching *CCC* values of approximately 0.98.

From the fitting results (Table 3), the largest canting errors predicted by the code are $\delta_{x2} = -4.69$ mrad in heliostat B6, $\delta_{y3} = 2.7$ mrad in D6, and $\delta_{y2} = -4.67$ mrad in F1. As expected, slope errors were in the range from 1 to 2 mrad.

In terms of computational cost, Table 4 presents the number of iterations required by the DIRECT algorithm to reach a converged solution. As stopping criteria, a small threshold of *CCC* variation over the last 10 iterations was considered. For heliostat A12, which presented the lowest optical quality, the algorithm provided a solution with fewer iterations and function evaluations than those of the remaining three heliostats. The function evaluation refers to the optical code that computes the flux mapping. On average, heliostat A12 also required fewer function evaluations per iteration than the rest. As can be seen in Visualization 1 for heliostat A12, in the first iterations, the algorithm quickly found the modules that provoke the separated spots. Ultimately, solutions for poorly canted heliostats are extracted with less computational cost.

In a laptop computer with an Intel Core i7-1065G7 microprocessor at 1.3 GHz and 8 GB of RAM memory, each function evaluation took an average of 0.093 s. Thus, for example, the F1 heliostat case required 13 min.

Optics EXPRESS

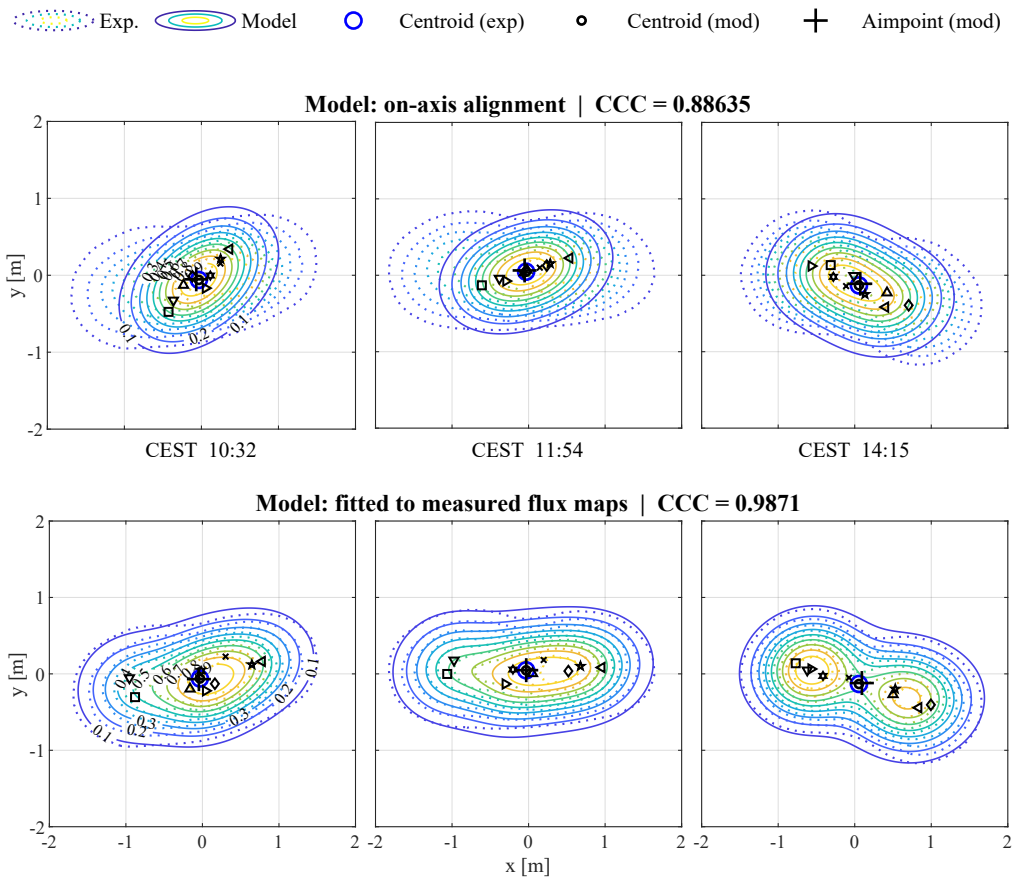

Fig. 9. Heliostat D6: experimental (dotted) and computed (solid lines) flux maps before (top) and after (bottom row) fitting.

Table 4. Computation metrics.

Heliostat	Iterations	Evaluations	Evals./it.
A12	50	4885	98
B6	80	12071	151
D6	60	10127	169
F1	60	8545	142

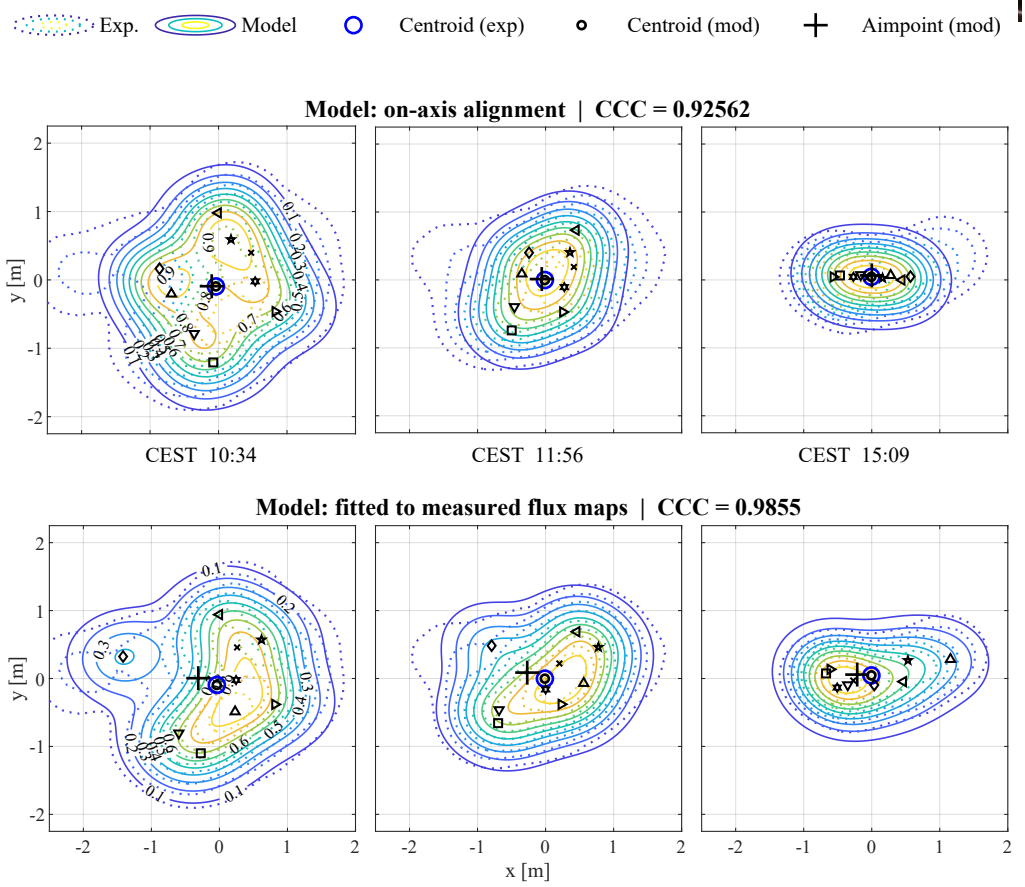

Fig. 10. Heliostat F1: experimental (dotted) and computed (solid lines) flux maps before (top) and after (bottom row) fitting.

5. Verification of aimpoint inference

A critical aspect of this alignment technique is the aimpoint inference, given that the heliostat orientation establishes the reference with respect to which canting errors are determined. This section describes a validation of the procedure to infer the aimpoint, as described in subSection 2.3.

Heliostat tracking is based on encoder systems for both azimuth and elevation positioning. As time passes, these systems lose their original reference with respect to the south and zero elevations. With the unknown pedestal tilt and the uncertainty of the sun position, this varying offset precludes a reliable measurement of the heliostat angles. As a consequence, a direct or indirect measurement of the instantaneous aimpoint is inaccessible.

Despite the absence of absolute heliostat angles, the variation of these angles between two time instants might be reliable. The angle variations can be calculated from the record of encoder counts. In CETHEL heliostats, each encoder –360 °– consists of 45150 counts. Therefore, the incremental angle is 0.00797342 ° per count.

The procedure to infer the aimpoint ultimately computes the normal vector of the heliostat. In spherical coordinates, the normal heliostat is described by azimuth (α) and elevation (ϵ) angles. Table 5 lists the computed α and ϵ for the four tested heliostats at the three time instants considered. Along with the model angles, the count number registered by the encoder is also provided in the same table. From the aforementioned incremental angle conversion, an indirect measurement of the heliostat angles can be achieved, although it is unrealistic because of the aforementioned offset issue.

Optics EXPRESS

Table 5. Azimuth (α) and elevation (ϵ) heliostat angles in terms of the model (aimpoint inference) in degrees and encoder counts (experimental measurement). Angles provided for each heliostat at three time instants.

Heliostat	Instant	Model [deg]		Exp. [Count #]	
		α	ϵ	α	ϵ
A12	#1	−45.8731	38.8446	−5700	4858
	#2	−37.7921	42.2832	−4676	5285
	#3	−14.4111	48.0267	−1741	5993
B6	1	−34.2004	52.2634	−4272	6533
	#2	−17.8296	54.8265	−2216	6852
	#3	22.3902	53.5560	2835	6697
D6	#1	−48.5532	33.4682	−6013	4237
	#2	−37.4746	38.7480	−4611	4898
	#3	−14.7155	44.4752	−1769	5611
F1	#1	−18.9613	43.1239	−2357	5462
	#2	−4.5938	45.0257	−550	5701
	#3	28.9354	41.4215	3655	5244

As previously explained, the angle difference between two successive time instants might be similar for both the model and the experiment. Table 6 lists the differences in azimuth ($\Delta\alpha$) and elevation ($\Delta\epsilon$). The deviations between the model and encoder differences in azimuth ($\Delta\alpha_m - \Delta\alpha_e$) and elevation ($\Delta\epsilon_m - \Delta\epsilon_e$) are included in the last two columns.

Table 6. Differences in azimuth ($\Delta\alpha$) and elevation ($\Delta\epsilon$) angles between consecutive time instants. Deviation between model (m) and experiment (e).

Heliostat	**Dif. instants**	**Model [deg]**		**Exp. [deg]**		**Deviation [deg]**	
		$\Delta\alpha$	$\Delta\epsilon$	$\Delta\alpha$	$\Delta\epsilon$	$\Delta\alpha_m - \Delta\alpha_e$	$\Delta\epsilon_m - \Delta\epsilon_e$
A12	#2 - #1	8.0811	3.4386	8.1648	3.4047	−0.0837	0.0340
	#3 - #2	23.3810	5.7435	23.4020	5.6452	−0.0210	0.0983
B6	#2 - #1	16.3708	2.5631	16.3934	2.5435	−0.0226	0.0196
	#3 - #2	40.2198	−1.2706	40.2738	−1.2359	−0.0539	−0.0347
D6	#2 - #1	11.0786	5.2798	11.1787	5.2704	−0.1001	0.0094
	#3 - #2	22.7591	5.7273	22.6605	5.6850	0.0986	0.0422
F1	#2 - #1	14.3675	1.9017	14.4080	1.9056	−0.0405	−0.0039
	#3 - #2	33.5291	−3.6042	33.5282	−3.6439	0.0009	0.0397

The largest deviation between the model and encoder corresponds to heliostat D6, precisely between the first and second time instants (0.1 °). The average deviation, in absolute value, between the model and encoder is 0.0439 °. In terms of encoder counts, the average deviation is smaller than the incremental angle of 6 counts.

Although the deviation between the model and experiment can be considered as small, two sources of deviation were identified. First, the encoder counts were manually registered immediately after image acquisition. The heliostat control at THEMIS is continuously correcting its orientation, which might lead to a slight difference between the actual and recorded counts. Second, because of encoder aging in THEMIS heliostats, its offset may vary within a single day.

Optics EXPRESS

6. Results and discussion

Once the flux-map fitting procedure predicted the canting errors, the heliostats were readjusted to correct their deviations. Thus, the performance of the proposed methodology was quantified and validated. After validation and discussion, the model was contrasted against raytracing results.

6.1. Correction and experimental validation

Heliostats A12, B6, D6, and F1 were adjusted according to the results presented in the previous section, specifically displayed in Table 3. The heliostat modules were recanted by adjusting the screw-nut arrangements that fasten the module frame to the main frame of the heliostats. Given the position of these supporting points and the metric of the screws, the angular deviations were converted into nut turns for the correction of canting deviations. It is important to note that the execution of recanting implies some imprecision, which is inherent to manual operations.

The adjustment of the mirror modules was performed between two and four days after the initial experimental campaign (Section 4). New heliostat images at the white target were acquired at three time instants similar to the initial ones (around noon, and two hours before and after noontime).

Figures 11–14 show the flux distributions before (top row) and after (bottom row) recanting in the four tested heliostats. The same contour color lines from 0.1 to 0.9 of normalized flux density are plotted. Solid lines correspond in this case to the actual measured images, and dotted lines map the model output for ideal alignment. The grayscale images corresponding to the top left corner of each time instant reproduce the real image acquired by the camera.

For heliostat A12, the original (before correction) multi-spot distribution was significantly improved, as can be seen in Fig. 11. By grouping the flux distribution into a single spot, it is clear that the fitting procedure adequately identified the mirror modules causing such disconnected beams. Small adjacent spots, such as those on the right in the afternoon, precluded achievin excellent optical quality. Nevertheless, the optical quality was remarkably increased in heliostat A12.

For heliostat B6, no noticeable improvement was found after adjustment, according to the computed canting deviations. The flux distribution differed with respect to the original one, but the optical quality did not seem to increase, according to the top and bottom images in Fig. 12.

Heliostat D6 showed acceptable optical quality in the initial experimental campaign. Small canting errors were detected by the fitting procedure, which improved the concentration of beam D6 after correction. As can be seen in Fig. 13, the originally very elongated spot (top row), tending to a two-peak pattern (afternoon image), became focused into a much more circular spot.

Lastly, the adjustment of heliostat F1 also enhanced its optical quality (Fig. 14). The original images showed small contiguous spots (e.g., the morning image), which were grouped into the central beam. As a result, the spot size was substantially reduced, thereby increasing the canting quality.

The cross-correlation coefficient constitutes a performance indicator of the canting quality. Experimental images can thus be compared with the ideal distributions from the model considering the on-axis alignment. Figure 15 presents the *CCC* values before and after the canting adjustment.

The largest improvement was achieved in heliostat A12, for which the original 0.635 correlation coefficient increased up to 0.87. Heliostats D6 and F1 also improved their flux distributions, reaching values above 0.98, very close to the maximum ($CCC = 1$).

By contrast, heliostat B6 decreased its *CCC* by 2 percentage points; consequently, the technique failed in this case. Although the canting methodology did not significantly worsen the optical quality of heliostat B6, the reasons for this lack of enhancement were investigated. The primary source of inaccuracy was attributed to defocus. As a matter of fact, heliostat B6 has the largest relative defocus among the tested heliostats.

Optics EXPRESS

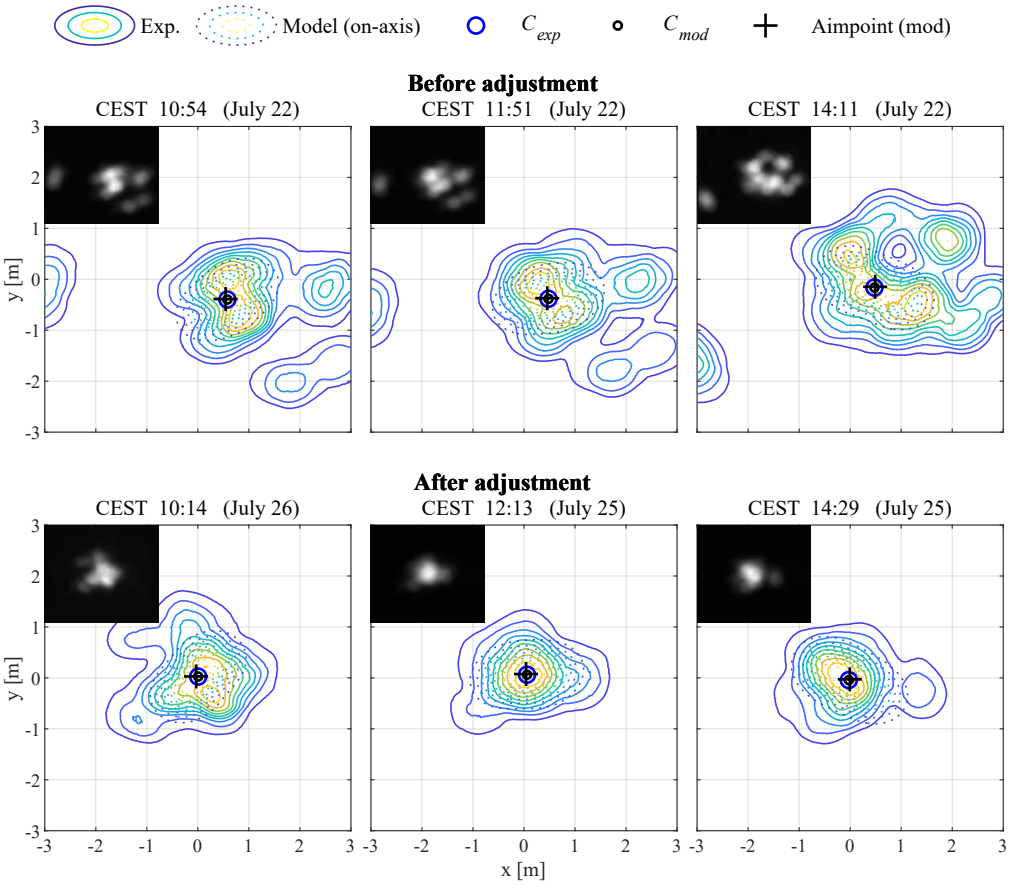

Fig. 11. Heliostat A12: experimental flux maps before (top) and after (bottom row) adjustment; dotted flux maps correspond to the on-axis model.

The presence of heliostat defocus on the target image is partly caused by the position of the white target, relatively far from the receiver aperture, at which heliostats are essentially aimed. In the THEMIS tower, the white target is 16.9 m below the center of the receiver aperture. Flux measurements closer to the receiver would be beneficial for the optical characterization of heliostats.

The analytic function at the image plane, on which the optical model is based, assumes perfect mirror focusing. Therefore, the astigmatic aberrations inherent to defocused mirrors are not reproduced by the model. Moreover, the UNIZAR function is appropriate for spherical mirrors, while the CETHEL mirror modules consist of three parabolic mirror strips that shape a quasi-spherical surface.

6.2. Comparison with raytracing

To show the aforementioned limitations of the convolution-projection model used in the present study, a comparison with a Monte-Carlo raytracing (MCRT) tool was carried out. For this task, the Solstice software [28] was employed.

The CETHEL heliostat, including its module's real geometry, was inputted in Solstice. A Gaussian sun-shape of 2.09 mrad and slope errors according to the optimization results (Table 3)

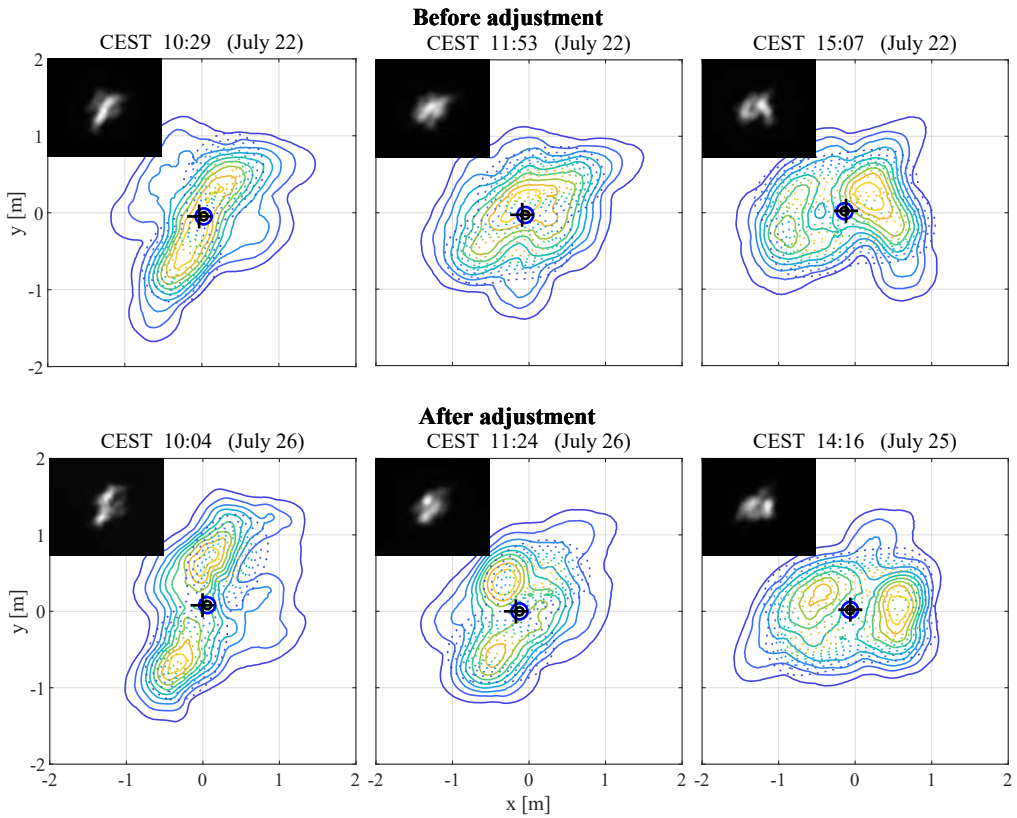

Fig. 12. Heliostat B6: experimental flux maps before (top) and after (bottom row) adjustment; dotted flux maps correspond to the on-axis model.

were considered, consistent with the values in the convolution-projection model. For proper comparison, on-axis canting was set in both tools.

For heliostats B6 (large defocus) and F1 (low defocus), Fig. 16 shows the flux maps generated by Solstice (solid contours) and the optical model (dotted). The three time instants in the after-adjustment scenario are represented. The greyscale background corresponds to the image captured by the camera.

Optics EXPRESS

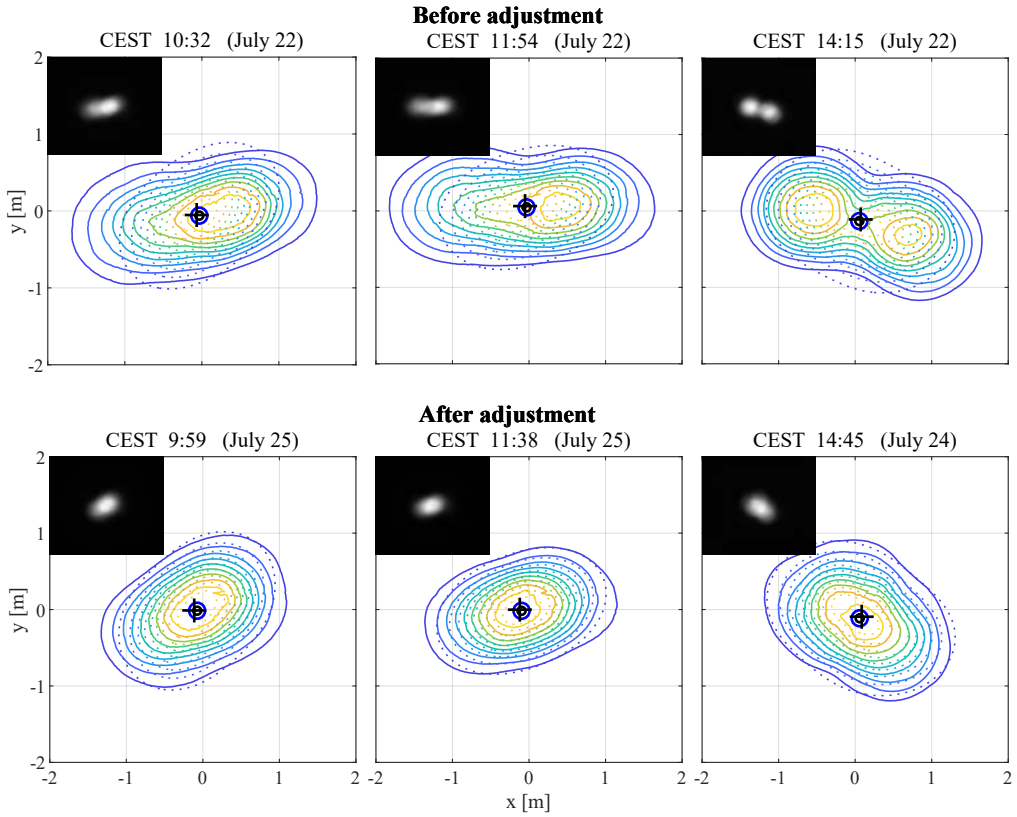

Fig. 13. Heliostat D6: experimental flux maps before (top) and after (bottom row) adjustment; dotted flux maps correspond to the on-axis model.

Optics EXPRESS

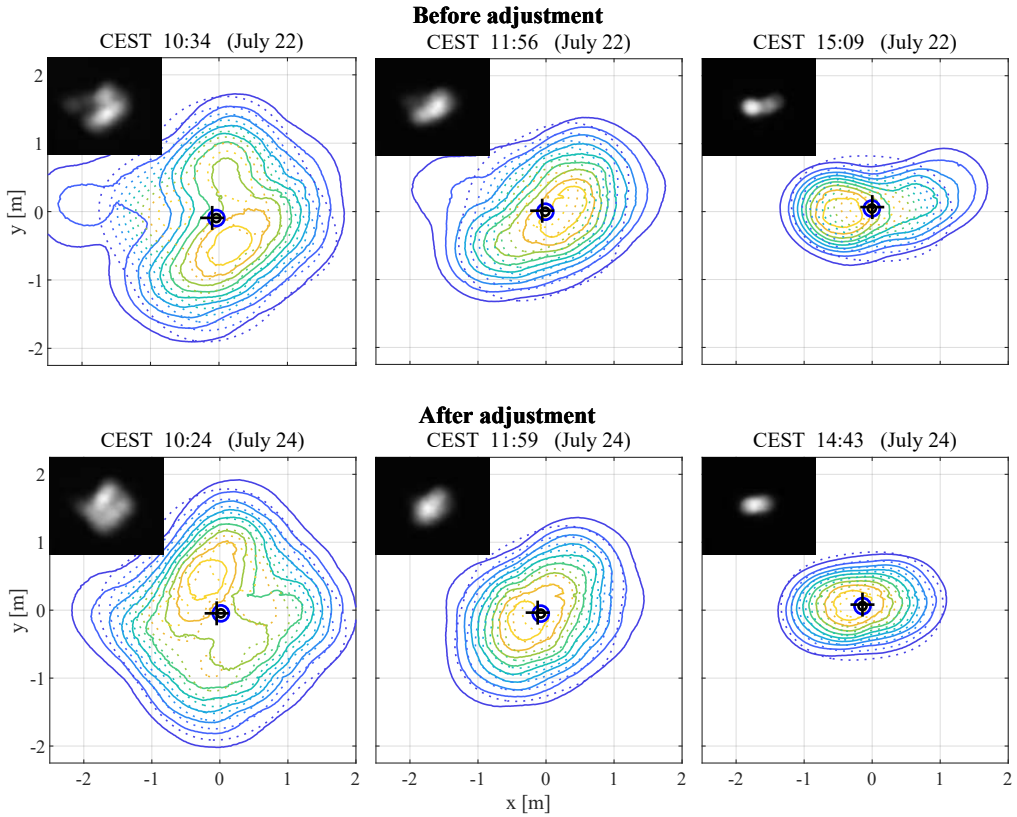

Fig. 14. Heliostat F1: experimental flux maps before (top) and after (bottom row) adjustment; dotted flux maps correspond to the on-axis model.

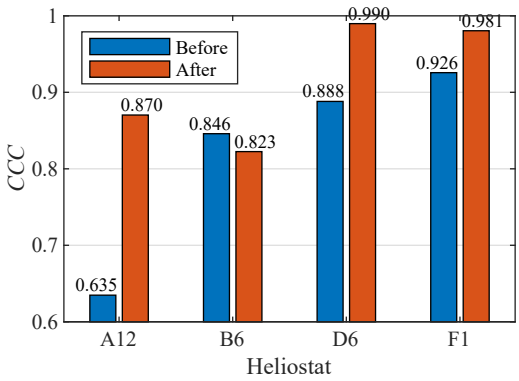

Fig. 15. Cross-correlation coefficients of the selected heliostats before and after adjustment.

From a closer inspection of the contours, note that the MCRT contours are invariably larger than those predicted by the model. This means that the spot size is greater than that predicted by the model, which is one of the effects arising from not being in the circle of minimum confusion (i.e., focused). As expected, this difference is larger for heliostat B6 (relative defocus: −43.1%) than for heliostat F1 (−15.7%).

Optics EXPRESS

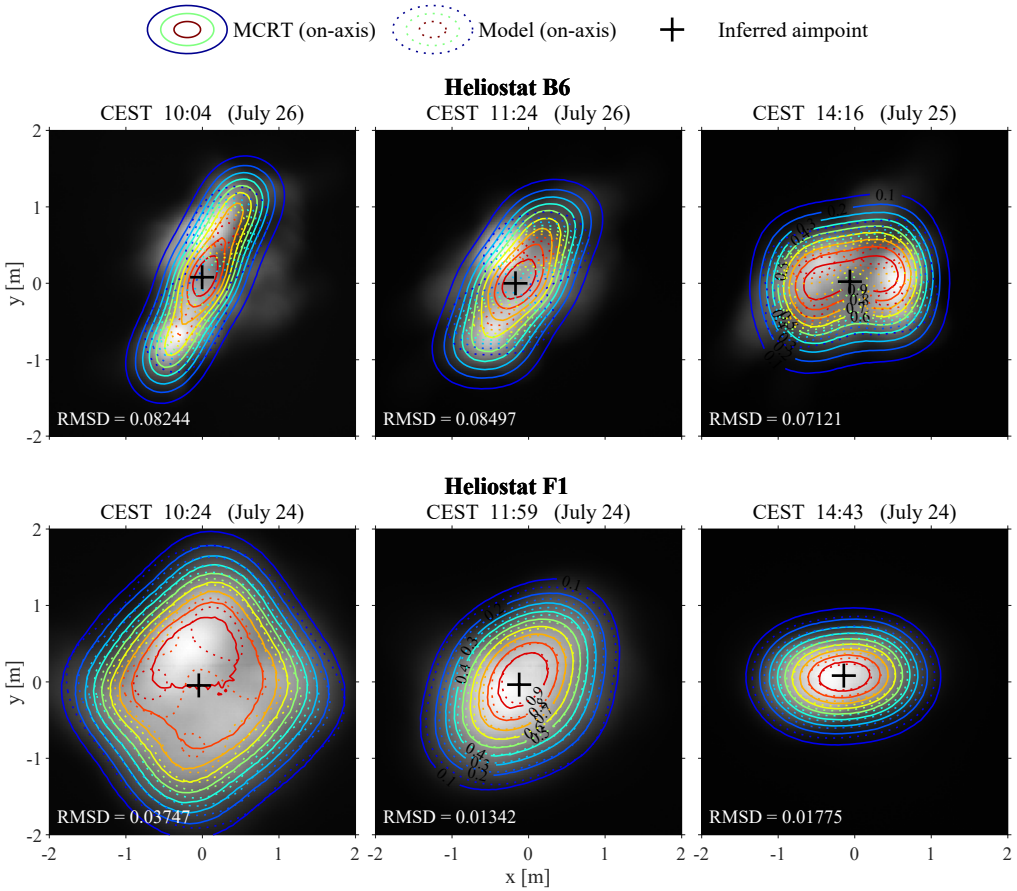

Fig. 16. Normalized flux maps by Solstice (solid) and the model (dotted contours) for heliostats B6 (top) and F1 (bottom row) with on-axis alignment. Background grayscale images show the experimental measurements after adjustment at three time instants.

To quantify the difference between the model and raytracing distributions, Fig. 16 provides the root mean square deviation (RMSD) at each instant. For heliostat B6, the *RMSD* is, on average, more than 3 times greater than that for heliostat F1.

This comparison shows the limitations of the convolution-projection model to address defocusing and non-spherical mirrors. Because of the reduction in the number of images resulting from the sensitivity analysis, the usage of raytracing within the framework of the presented technique deserves further investigation.

7. Conclusions

A flux map fitting procedure was implemented to identify canting errors in real heliostats. By matching the computed flux maps to the measured ones, canting deviations were found in the modules of four heliostats at the THEMIS solar tower.

The cross-correlation coefficient between the measured and modeled maps was utilized as the objective function to maximize. The DIRECT algorithm was found to lead to deterministic results, regardless of the starting point and without the need for parameter tuning.

Optics EXPRESS

A preliminary sensitivity analysis was performed to determine an appropriate separation between image captures to feed the algorithm. An approximately constant variation of the sun position between images was considered to generate several sets of images with different number of them. From the conducted sensitivity analysis, which cannot be generalized for other heliostat types, three experimental images spread along a single day (i.e., morning, noon, and afternoon) were selected. A larger number of images increases the computation time without guaranteeing a more accurate result.

In the absence of a precise measurement of the solar position and pedestal tilt, a methodology to determine the heliostat aimpoint was developed. This procedure was verified against data from heliostat tracking encoders. By considering the increments in azimuth and elevation angles between consecutive time instants, the deviation between the model inference and encoder was 0.0439 ° on average, equivalent to less than 6 encoder counts.

The proposed methodology was validated with four selected heliostats, which were recanted according to the deviations resulting from the optimization. From a visual inspection of the heliostat images before and after adjustment, the optical quality was clearly improved in three of them. The most notable case is that of heliostat A12, initially with a very poor canting (CCC = 0.635), for which the multiple and separated spots were centered into a single spot (CCC = 0.87). In heliostats D6 and F1, originally with a fair canting quality, the CCC values exceeded 0.98. By contrast, heliostat B6 did not improve its optical quality. In fact, the CCC slightly decreased from 0.846 to 0.823.

The canting failure for heliostat B6 is attributed to the difference between slant range and focal length, given that heliostat B6 presents a high relative defocus of −43%. The optical model utilized in the presented study, which is based on an analytic function, properly reproduces neither the defocus phenomena nor non-spherical mirror geometry. These limitations emerged when comparing with the Solstice raytracing tool. This comparison evidenced the spot widening caused by defocus.

In summary, the presented canting procedure exhibited a satisfactory success rate (three to four) to improve the optical quality of misaligned heliostats substantially. However, conducting tests on a larger number of heliostats might be required to obtain statistically valid results. In the event of a large mirror defocus, the reliability can be undermined. Raytracing tools can be implemented on this technique to overcome the limitations encountered in the convolution-projection model.

Funding

Universidad Carlos III de Madrid (2020/00051); European Commission (823802); Horizon 2020 Framework Programme (727762).

Acknowledgments

We thank the CNRS-PROMES laboratory, UPR 8521, belonging to the French National Center for Scientific Research (CNRS), for providing access to its facilities, the support of its scientific and technical staff, and the financial support of the SFERA-III project (Grant Agreement No. 823802). We thank the technical help provided by Yann Volut, William Baltus, and Antoine Pérez. The research project VISHELIO-CM-UC3M has been funded by the call "Programa de apoyo a la realización de proyectos interdisciplinares de I+D para jóvenes investigadores de la Universidad Carlos III de Madrid 2019-2020" under the framework of the "Convenio Plurianual Comunidad de Madrid-Universidad Carlos III de Madrid". This project has received funding from the European Union's Horizon 2020 research and innovation program under grant agreement No. 727762, project acronym NEXT-CSP.

Optics EXPRESS

Disclosures

The authors declare no conflicts of interest.

References

1. K. M. Hampson, D. Gooding, R. Cole, and M. J. Booth, "High precision automated alignment procedure for two-mirror telescopes," Appl. Opt. **58**(27), 7388 (2019).
2. J. M. Pasachoff and W. Livingston, "Coelostat and heliostat: alignment and use for eclipse and other field purposes," Appl. Opt. **23**(16), 2803 (1984).
3. R. Winston, J. C. Mi nano, and P. Benítez, *Nonimaging Optics* (Elsevier, 2005).
4. M. Coquand, F. Henault, and C. Caliot, "Backward-gazing method for measuring solar concentrators shape errors," Appl. Opt. **56**(7), 2029 (2017).
5. L. L. Vant-Hull, "Central tower concentrating solar power (CSP) systems," in *Concentrating solar power technology: principles, developments and applications*, (Woodhead Publishing - Elsevier, 2012), chap. 8.
6. D. Buie, C. J. Dey, and S. Bosi, "The effective size of the solar cone for solar concentrating systems," Sol. Energy **74**(5), 417–427 (2003).
7. Y. Wang, D. Potter, C.-A. Asselineau, C. Corsi, M. Wagner, C. Caliot, B. Piaud, M. Blanco, J.-S. Kim, and J. Pye, "Verification of optical modelling of sunshape and surface slope error for concentrating solar power systems," Sol. Energy **195**, 461–474 (2020).
8. S. A. Jones, "Annual performance prediction for off-axis aligned Lugo heliostats at Solar Two," in *American Society of Mechanical Engineers international solar energy conference*, Sandia National Laboratories (SAND-96-0212C, San Antonio, TX (United States), 1996).
9. J. Yellowhair and C. K. Ho, "Heliostat Canting and Focusing Methods: An Overview and Comparison," in *ASME 2010 4th International Conference on Energy Sustainability*, Volume 2, (ASME, 2010), pp. 609–615.
10. L. Ren, X. Wei, Z. Lu, W. Yu, W. Xu, and Z. Shen, "A review of available methods for the alignment of mirror facets of solar concentrator in solar thermal power system," Renewable Sustainable Energy Rev. **32**, 76–83 (2014).
11. M. Röger, C. Prahl, and S. Ulmer, "Fast determination of heliostat shape and orientation by edge detection and photogrammetry," presented at *SolarPaces*, Las Vegas, NV, 2008.
12. S. A. Jones, R. M. Edgar, and R. M. Houser, "Recent results on the optical performance of solar two heliostats," in *American Society of Mechanical Engineers international solar energy conference*, Sandia National Laboratories (SAND-94-2776C, Lahaina, HI (United States), 1994).
13. E. Sproul, K. Chavez, and J. Yellowhair, "The Development of the Heliostat Focusing and Canting Enhancement Technique: An Optical Heliostat Alignment Tool for the National Solar Thermal Test Facility," in *ASME 2011 5th International Conference on Energy Sustainability, Parts A, B, and C*, (ASME, 2011), pp. 611–619.
14. A. Sánchez-González and J. Yellowhair, "Reflections between heliostats: Model to detect alignment errors," Sol. Energy **201**, 373–386 (2020).
15. A. Sánchez-González, C. Caliot, A. Ferriere, and D. Santana, "Determination of heliostat canting errors via deterministic optimization," Sol. Energy **150**, 136–146 (2017).
16. J. Ballestrín, M. Carra, R. Enrique, R. Monterreal, J. Fernández-Reche, J. Polo, M. Casanova, F. Barbero, and A. Marzo, "Diagnosis of a Lambertian target in solar context," Measurement **119**, 265–269 (2018).
17. M. Weber, M. Fink, V. Fortov, A. Lipaev, V. Molotkov, G. Morfill, O. Petrov, M. Pustylnik, M. Thoma, H. Thomas, A. Usachev, and C. Raeth, "Assessing particle kinematics via template matching algorithms," Opt. Express **24**(8), 7987 (2016).
18. D. R. Jones, C. D. Perttunen, and B. E. Stuckman, "Lipschitzian optimization without the Lipschitz constant," J. Optimiz Theory App. **79**(1), 157–181 (1993).
19. D. E. Finkel, "DIRECT Optimization Algorithm User Guide," (2003).
20. L. Li, J. Coventry, R. Bader, J. Pye, and W. Lipiński, "Optics of solar central receiver systems: a review," Opt. Express **24**(14), A985–A1007 (2016).
21. A. Sánchez-González and D. Santana, "Solar flux distribution on central receivers: A projection method from analytic function," Renewable Energy **74**, 576–587 (2015).
22. A. Sánchez-González, M. R. Rodríguez-Sánchez, and D. Santana, "Aiming factor to flatten the flux distribution on cylindrical receivers," Energy **153**, 113–125 (2018).
23. F. Collado, A. Gómez, and J. Turégano, "An analytic function for the flux density due to sunlight reflected from a heliostat," Sol. Energy **37**(3), 215–234 (1986).
24. F. Biggs and C. N. Vittitoe, "Helios model for the optical behavior of reflecting solar concentrators," Tech. rep., Sandia National Laboratories, SAND-76-0347 (1979).
25. M. Schmitz, P. Schwarzbözl, R. Buck, and R. Pitz-Paal, "Assessment of the potential improvement due to multiple apertures in central receiver systems with secondary concentrators," Sol. Energy **80**(1), 111–120 (2006).
26. USNO, "Solar position," Online calculator (2016).
27. M. J. Blanco, D. C. Alarcon-padilla, and T. Lopez, "Computing the solar vector," Sol. Energy **70**(5), 431–441 (2001).
28. C. Caliot, H. Benoit, E. Guillot, J.-L. Sans, A. Ferriere, G. Flamant, C. Coustet, and B. Piaud, "Validation of a Monte Carlo Integral Formulation Applied to Solar Facility Simulations and Use of Sensitivities," J. Sol. Energy Eng. **137**(2), 021019 (2015).